Formation of SiP 2 Nanocrystals Embedded in SiO 2 from Phosphorus-Rich SiO 1.5 Thin Films

S. Geiskopf, Mathieu Stoffel, X. Devaux, Erwan André, C. Carteret, A. Bouché, Michel Vergnat, Hervé Rinnert

▶ **To cite this version:**

S. Geiskopf, Mathieu Stoffel, X. Devaux, Erwan André, C. Carteret, et al.. Formation of SiP 2 Nanocrystals Embedded in SiO 2 from Phosphorus-Rich SiO 1.5 Thin Films. Journal of Physical Chemistry C, 2020, 124 (14), pp.7973-7978. 10.1021/acs.jpcc.9b11416 . hal-02931700

HAL Id: hal-02931700
https://hal.science/hal-02931700v1

Submitted on 12 Nov 2020

HAL is a multi-disciplinary open access archive for the deposit and dissemination of scientific research documents, whether they are published or not. The documents may come from teaching and research institutions in France or abroad, or from public or private research centers.

L'archive ouverte pluridisciplinaire **HAL**, est destinée au dépôt et à la diffusion de documents scientifiques de niveau recherche, publiés ou non, émanant des établissements d'enseignement et de recherche français ou étrangers, des laboratoires publics ou privés.

Formation of SiP_2 nanocrystals embedded in SiO_2 from phosphorus rich $SiO_{1.5}$ thin films

S. Geiskopf [1], M. Stoffel[1,*], X. Devaux[1], E. André[2], C. Carteret[2], A. Bouché[1],

M. Vergnat[1], H. Rinnert[1]

[1] *Université de Lorraine, CNRS, IJL, F-54000 Nancy, France*

[2] *Université de Lorraine, UMR CNRS 7564, LCPME, 405 rue de Vandœuvre,*

54600 Villers-lès-Nancy, France

Abstract

We investigate the structural, vibrational and optical properties of phosphorus-rich $SiO_{1.5}$ thin films annealed at 1100°C. For phosphorus (P) contents larger than 3 at. %, high resolution transmission electron microscopy characterizations reveal the presence of both spherical shaped SiP_2 nanoparticles crystallizing in an orthorhombic structure and bumps in epitaxy with the underlying Si substrate. Energy dispersive spectroscopy measurements confirm the SiP_2 stoichiometry. Moreover, electron energy loss spectroscopy characterizations allow us to determine the exact location of P and Si atoms. Apart from SiP_2 nanoparticles, P atoms are found to be located in the bumps and in the Si substrate to a level of 1 at. %, which is explained by P diffusion during annealing. The vibrational properties determined by Raman spectroscopy are found to be in excellent agreement with density functional theory calculations of the vibration modes for the SiP_2 alloy. Finally, the quenching of the photoluminescence with the increasing P content is explained on the basis of the structural data.

Si nanocrystals (Si-NCs) have been extensively studied during the last two decades due to their original electronic and optical properties. Additional functionalities can be expected if the nanocrystals can be effectively doped. This is, however, a challenging issue which is related with several physical and technological barriers. In particular, the increasing formation energy for substitutional dopants with the decreasing size can lead to a "self-purification" mechanism for small nanocrystals [1]. Nevertheless, both P and B doped Si nanocrystals embedded in a SiO_2 matrix have been successfully obtained by high temperature phase separation of Si rich SiO_x thin films deposited by e-beam evaporation [2], plasma enhanced chemical vapor deposition [3], ion implantation [4] or by using a combination of the two last techniques [5]. Another important question concerned the localization of the dopants. König et al. [6] used atom probe tomography to demonstrate that in the case of P-doped Si nanocrystals embedded in SiO_2 prepared by plasma enhanced chemical vapor deposition, only 15 % of the P atoms are found within the nanocrystals while 30 % are localized at the interface with the SiO_2 matrix and 55% in the silica matrix. Alternatively, ion beam synthesis by silicon/dopant co-implantation appeared to be a viable route to obtain a high concentration of P atoms inside Si nanocrystals [4]. Very recently, it has been shown both theoretically [7] and experimentally [8-11] that either phosphorus or boron doped Si-NCS can be of interest for tunable localized surface plasmon resonances (LSPR). When the dopant concentration is very high, the solid solubility limit could be exceeded and alloying could become possible. Indeed, the Si-P equilibrium phase diagram established so far predicts that two stable compounds may form (SiP and SiP_2) depending on the relative amount of phosphorus [12-14]. Both orthorhombic and pyrite type bulk SiP_2 alloys were first synthesized by Wadsten in 1967 [15,16]. Donohue et *al.* [17] refined the structure of pyrite type SiP_2 by using X-ray powder diffraction. Based on galvanomagnetic and reflectance measurements, these authors claim that pyrite-type SiP_2 could be a semimetal. Farberovich *et al.* [18] came to the same

conclusion by calculating the band structure using the orthogonalized plane wave method. Vogt et *al.* [19] characterized the vibrational properties of pyrite type SiP_2 and obtained the frequencies of all Raman active phonons at room temperature. Meier et *al.* [20] performed *ab initio* calculations of the fundamental vibration frequencies of pyrite type SiP_2. A good agreement was found with both Raman and infrared studies. Bachhuber at *al.* [21] further used first principle calculations to investigate the structure, the bonding and the vibrational properties of pyrite type SiP_2. By using the vapor transport method, SpringThorpe [22] succeeded to prepare single crystals of orthorhombic SiP_2. This compound was shown to be a p-type semiconductor with an optical bandgap of about 1.89 eV. By using the Sn flux method with Gd as a mineralizer in a fused silica tube, Zhang et *al.* [23] identified by means of X-ray diffraction another orthorhombic phase of SiP_2 crystallizing in the *Pnma* group. Diffuse reflectance measurements as well as preliminary density functional theory (DFT) calculations suggest a semiconducting behavior with a bandgap close to 1.4 eV. Moreover, SiP_2 microparticles prepared by ball milling [24] but also nanocomposites consisting of SiP_2 and amorphous carbon as well as carbon nanotube wrapped SiP_2 [25] emerged as promising anode materials for high performance Li-and Na-ion batteries [26,27].

Very recently, Si_xP_y alloys (x,y =1,2) have gained a renewed interest since they exhibit a lamellar structure. This property might be of interest for engineering novel Si-based 2D materials, which could allow filling the gap between silicene and phosphorene. Density functional theory (DFT) calculations have shown that 2D-SiP_x (x = 1, 2) are direct bandgap semiconductors [28-31], which might be of particular interest for future optoelectronic applications. Moreover, according to its band structure, 2D-SiP_2 appears to be promising for photocatalytic water splitting [31].

Till now, there are no reports available in the literature concerning the growth of orthorhombic SiP_2 either in thin films or nanocrystals. In this paper, we demonstrate the

formation of orthorhombic SiP_2 nanocrystals embedded in silicon dioxide thin films obtained by annealing of phosphorus rich $SiO_{1.5}$ thin films at 1100°C. We provide a careful structural and vibrational study of SiP_2 nanocrystals. The experimental results are found to be in excellent agreement with density functional theory calculations of the vibration modes for the SiP_2 alloy. The optical properties of P-rich $SiO_{1.5}$ thin films are further discussed in relation with the obtained structural results.

Phosphorus-rich $SiO_{1.5}$ thin films were prepared by co-evaporation on Si(001) substrates held at room temperature of SiO and SiO_2 from e-beam guns and P from a GaP decomposition source [32]. The SiO and SiO_2 fluxes were controlled by a quartz microbalance. The P content, which is defined by [P]/([Si]+[O]+[P]), was obtained by comparing the relative intensities of the P *2p*, Si *2p* and O *1s* core levels measured using X-ray photoelectron spectroscopy (XPS). The obtained values were cross-checked by secondary ion mass spectroscopy (SIMS) measurements. The total film thickness was about 200 nm for all samples considered in this study. The samples were post-grown annealed in a rapid thermal annealing furnace at 1100°C during 5 minutes under N_2 atmosphere. The structural properties of the samples were investigated by high resolution transmission electron microscopy (HRTEM), scanning transmission electron microscopy (STEM), energy dispersive spectroscopy (EDS) and electron energy loss spectroscopy (EELS) using a JEOL ARM 200 F probe corrected with cold field emission gun. EELS spectrum images were recorded with a Gatan GIF quantum ER filter. To avoid any phase precipitation due to ion or electron beam damages, the samples were mechanically thinned up to the electron transparency by the tripod method and the TEM was operated at 80 kV with a probe current lower than 70 pA for EDS and EELS spectrum images. For EELS investigations, zero-loss and core-loss spectrum images were recorded simultaneously to allow advanced data post processing (correction of energy drift, thickness correction). To separate overlapping Si edges

and P edges and chemical states of Si and extract quantitative data, multiple linear least square fitting (MLS) was used using reference spectra recorded on pure Si and on pure thermal silica grown on a Si wafer. The reference spectra were recorded with the same STEM and spectrometer parameters than that of the sample investigated. Raman scattering measurements were performed at RT by using a 532 nm laser diode as excitation source. The scattered light is analyzed by a monochromator equipped with a 1800 lines/mm grating and a CCD detector. The steady state photoluminescence was excited with a 325 nm He-Cd laser and subsequently analyzed by a monochromator equipped with a 600 grooves/mm grating and measured by a photomultiplier tube operating in the visible-IR range. The spectra were corrected from the response of the detector. Density functional theory (DFT) calculations were performed with the CRYSTAL14 [33] periodic computation code using the B3LYP functional [33, 34] and a triple ζ localized (atom centered) basis set [35]. Both the atomic positions and the cell parameters of SiP_2were optimized. The harmonic vibration frequencies were calculated at the Γ point and the corresponding intensities were evaluated through a coupled perturbed Kohn-Sham (CPKS) approach.

Figure 1 (a) shows a HRTEM image of a $SiO_{1.5}$ thin film containing 10 at. % of phosphorus after annealing for 5 minutes at 1100°C. Two kinds of features can be distinguished. Firstly, the interface with the substrate is not sharp but one can identify bumps which are in epitaxy with the substrate. A high resolution STEM-high angle annular dark field (HAADF) image of the interface between a typical bump and the Si substrate is shown in Fig. 1(b). The zone axis of the Si substrate is <110>. The interface is indicated by a red dash-dotted line. One can clearly identify the dumbbell of Si <110> both in the bump and in the substrate showing that the bumps are in epitaxy with the underlying Si substrate. Secondly, in the thin film, one can distinguish large, spherical shaped nanoparticles having typical sizes between 30 and 40 nm. One can clearly distinguish the atomic planes demonstrating almost perfect crystallinity. We

note, however, that these nanocrystals often contain a high density of twins and stacking faults. Similar particles can also be identified in samples containing 3 and 6 at. % of phosphorus (not shown here). Their size increases from about 12 nm in the film containing 3 at. % of phosphorus to 31 nm in the film containing about 10 at. % of phosphorus. Figure 1(c) displays a Fourier transform of the spherical nanocrystal identified in Figure 1(a). A simulation of the electron diffraction pattern of SiP_2 with *Pbam* orthorhombic structure (JCPDS file 00-044-1124) was compared to the Fourier transform. A good agreement is found for the zone axis [014]. This is the first experimental observation of SiP_2 nanocrystals crystallizing in an orthorhombic structure. In order to characterize the chemical composition of both types of nanostructures, we have performed EDS spectrum images (SI). Figure 2 shows a HAADF image (Fig. 2(a)) together with the chemical semi-quantitative maps for Si (Fig. 2(b)), O (Fig. 2(c)) and P (Fig. 2(d)) extracted from EDS-SI. The EDS spectra extracted from EDS-SI in three different regions (delimitated in Figs. 2(b), 2(c) and 2(d)) are shown in Figure 2(e). Three different peaks can be identified at 0.5, 1.7 and 2.0 keV corresponding to the Kα emission lines of oxygen, of silicon and of phosphorus, respectively. In the substrate, one can find about 1 at. % of phosphorus indicating that P diffusion has occurred during annealing at 1100°C. Moreover, the EDS spectrum extracted from the bump area shows that the bumps contain also about 1 at. % of phosphorus. The oxygen related peak at 0.5 keV originates from SiO_2 which is present both on top and below the bump. Finally, for the large nanocrystals, the Si-related peak at 1.7 keV originates from both Si atoms located in SiO_2 and in SiP_2. Indeed, under the electron probe, X-rays are emitted from the whole thickness of the sample. Consequently, Si atoms in SiO_2 present both on top and below the nanocrystals will also emit. To obtain the real Si content in the nanoparticles, the contribution resulting from Si atoms present in SiO_2 have to be subtracted. This can be done easily by assuming that all oxygen atoms originate from the stoichiometric SiO_2 compound. A Si content of about 32.8

at. % and a phosphorus content of 67.2 at. % was then obtained, which is compatible with the presence of a SiP_2 compound. However EDS measurements do not allow to distinguish clearly between silicon atoms in SiP_2 nanoparticles, in silicon bumps and in the silicon dioxide matrix. Moreover, the EDS signal is known to be not fully localized. In order to get a more precise chemical mapping at the nanoscale and to be able to distinguish between $Si^{(0)}$ and $Si^{(4+)}$, we have performed further STEM-EELS spectrum images. Figure 3(a) shows a STEM-HAADF image of an annealed film containing 10 at. % of phosphorus annealed at 1100°C. One can clearly distinguish both the nanoparticles and the bumps. Figure 3(b) shows an EELS spectrum integrated over the whole area shown in Fig. 3(a) (black solid line). To get a chemical map, we have performed a minimum least square fitting of this spectrum by using reference spectra for $Si^{(0)}$ and $Si^{(4+)}$ (from a lamella of thermal SiO_2 grown by oxidation of Si(100)) measured in the same experimental conditions (thickness, accelerating voltage, probe current, convergence and collection angle, etc.). Moreover, the fitting leads to a residual spectrum (orange solid line in figure 3(b) having an edge at 129 eV, which corresponds to phosphorus [36]. By considering the reference spectra for both $Si^{(0)}$ and $Si^{(4+)}$ and the residual spectrum for phosphorus, we were able to reconstruct the chemical map for each element with a new MLS fitting of each pixel of the SI. Figure 3(c)-(d) show the chemical maps for both $Si^{(0)}$ and P. One can recognize that Si is present in the substrate, in the bumps and in the nanocrystals. P atoms are localized in the nanocrystals and at the interface between the substrate and the film, which originates from P diffusion during annealing. It is noteworthy that the maps for Si and P superimpose perfectly in the thin films indicating that both Si and P atoms are located in the nanocrystals. Full EELS chemical maps showing $Si^{(0)}$, $Si^{(4+)}$ and P as well as the superposition of maps is presented in the Supplementary Information (Fig. S1). Finally, one can discuss briefly the formation of the bumps at the interface with the substrate. In case of pure $SiO_{1.5}$ films, they are not observed. Their size and height increases as the P

content in the films increases. During annealing at high temperatures, both P atoms and Si atoms in excess which do not participate in either SiP_2 or SiO_2 will diffuse towards the substrate. The diffusion will be even enhanced for larger P contents thus leading to formation of larger bumps. The Si atoms eventually accumulate into holes created in the oxide at the interface thus leading to the formation of bumps in epitaxy with the Si(001) substrate.

All the previous characterizations were done at the nanometer scale. To obtain a spectroscopic signature of the SiP_2 nanocrystals, we have further performed Raman scattering measurements. Figure 4 (a) shows Raman spectra measured for $SiO_{1.5}$ thin films with various P contents ranging from 0.3 at.% to 10 at. % and annealed at 1100°C. The films were deposited onto silica substrates in order to get rid of the huge signal originating from the Si-TO line at 520.5 cm^{-1}. For P contents below 3 at. %, the spectra are essentially dominated by the signal originating from the silica substrate. However, for P contents of about 10 at. %, new and sharp peaks can be observed suggesting the formation of a new crystalline phase. According to all structural results from this work, these peaks could possibly be a signature of the SiP_2 compound. To clarify the origin of these peaks, we have performed DFT calculations of the vibrational modes for the orthorhombic SiP_2 structure. Figure 4 (b) shows the experimental spectrum (blue solid line) as well as the calculated Raman spectra for the orthorhombic SiP_2 alloy (magenta solid line). It is obvious that a good agreement is obtained between the experimental and the calculated Raman spectrum thus further confirming that the observed nanocrystals consist indeed of SiP_2. Table I summarizes the position of both calculated and measured vibrational wavenumbers. Some differences appear nevertheless between the theoretical and the experimental values, which could be due either to the approximations used for the DFT calculations or to the fact that a non-negligible strain may be exerted by the silica matrix onto the SiP_2 nanocrystals. The different vibrational modes are

also identified next to the calculated vibrational wavenumbers. Finally, our structural investigations help to shed new light on the evolution of the photoluminescence of $SiO_{1.5}$:P thin films with increasing P contents. Figure 5 displays the room temperature PL spectra measured for $SiO_{1.5}$ thin films with various P contents ranging from 0.3 at.% to 10 at. %. For the lowest P content (i.e. 0.3 at.%), the PL signal is characterized by a rather broad band extending from about 700 nm to 1000 nm. In this particular sample, SiP_2 nanocrystals could not be detected. The observed luminescence thus originates from radiative recombinations between charge carriers confined in pure Si nanocrystals. For the sample containing about 3 at. % of P, a strong decrease of the PL intensity is observed. Similar evolutions have been reported in the literature and are generally ascribed to the Auger effect [37] in Si-NCs containing P atoms which could then act as dopants. Spatially resolved EELS measurements performed on the same sample (see Fig.S1, Supplementary Informations) revealed the coexistence of both SiP_2 nanocrystals having typical sizes of about 15 nm and Si nanocrystals with sizes ranging between 4 and 6 nm. Only few of them have sizes below the Bohr radius of the exciton in bulk Si and can contribute to the observed photoluminescence thus explaining the strong intensity decrease when the P content increases from 0.3 at. % to 3 at. % of P. Moreover, the PL peak shifts to larger wavelength thus suggesting an increase of the Si nanocrystal size, which is indeed observed. Finally, no PL could be detected for the sample having the highest P content (i.e. 10 at. %). In this case, all Si atoms are either involved in the SiP_2 nanocrystals or in the bumps at the interface with the substrate.

To summarize, we provided clear evidence of the formation of SiP_2 nanocrystals in P-rich $SiO_{1.5}$ thin films annealed at 1100°C. The latter are found to crystallize in an orthorhombic structure. Elemental chemical mapping confirmed the SiP_2 stoichiometry and allowed us to determine the exact location of both P and Si atoms. Apart from the SiP_2 nanocrystals, P atoms are located in Si bumps, which are in epitaxy with the substrate, and at

the substrate surface to a level of about 1 at. %. The vibrational properties are found to be in excellent agreement with DFT calculations of the vibrational modes for the SiP_2 alloy. Finally, the photoluminescence properties of $SiO_{1.5}$ thin films with various P contents in the range 0.3-10 at. % can be understood by considering the structural properties. Our results shed new light into the complex evolution of ternary Si-O-P alloys during high temperature annealing.

Acknowledgments

The authors would like to acknowledge the LUE (Lorraine Université d'Excellence) and the CPER MatDS projects for support.

Figure captions:

Figure 1: (a) HRTEM image of a $SiO_{1.5}$ thin film containing 10 at. % of P annealed at 1100°C for 5 minutes. (b) HRSTEM-HAADF image of the interface between a typical bump and the Si substrate. One can identify the [110] dumbbell of Si. The substrate is oriented along the <110> zone axis for all images. The interface is indicated by a red dash-dotted line. The intensity difference between the substrate and the bump is due to the presence of silica above and below the bump. (c) Fourier transform of the nanocrystal delimitated by a red dash-dotted line in (a).

Figure 2: (a) STEM-HAADF image of a $SiO_{1.5}$ thin film containing 10 at. % of P annealed at 1100°C for 5 minutes. Quantitative chemical maps drawn from Si K (b), O K (c) and P K (d) signals. (e) EDS spectra extracted in SI from the different square zones indicated in (a)-(d).

Figure 3: (a) Spectrum image of a $SiO_{1.5}$ thin film containing 10 at. % of P annealed at 1100°C for 5 minutes. (b) EELS spectrum of the sample (black solid line) together with reference spectra relative to Si^{4+} (cyan), Si^{0} (red) and P (orange). K edges maps for $Si^{(0)}$ (c) and P (d) resulting from the MLS fitting

Figure 4: (a) Raman spectra of $SiO_{1.5}$ thin films with different P contents annealed at 1100°C for 5 minutes. The films were grown onto silica substrates. (b) Experimental Raman spectrum of a $SiO_{1.5}$ thin film containing 10 at. % of P (blue solid line) and calculated spectrum for SiP_2 (magenta solid line)

Table I: Measured (ω_{EXP}) and calculated (ω_{DFT}) vibrational wavenumbers of orthorhombic SiP_2. The symmetry species of the vibrational modes are indicated in brackets.

Figure 5: Room temperature photoluminescence spectra of $SiO_{1.5}$ thin films with different P contents ranging between 0.3 at. % and 10 at. %. The spectra relative to the samples containing 3 at. % and 10 at. % of P have been multiplied by 10.

References:

[1] Dalpian G. M.; Chelikowsky J. R., Self purification in semiconductor nanocrystals, Phys. Rev. Lett. **96**, 226802 (2006)

[2] Perego M.; Bonafos C.; Fanciulli M., Phosphorus doping of ultra-small silicon nanocrystals, Nanotechnology **21**, 025602 (2010)

[3] Gutsch S.; Laube J.; Hiller D.; Bock W.; Wahl M.; Kopnarski M.; Gnaser H.; Puthen-Veettil B.; Zacharias M., Electronic properties of phosphorus doped silicon nanocrystals embedded in SiO_2, Appl. Phys. Lett. **106**, 113103 (2015)

[4] Khelifi R.; Mathiot D.; Gupta R.; Muller D.; Roussel M.; Duguay S., Efficient n-type doping of Si nanocrystals embedded in SiO_2 by ion beam synthesis, Appl. Phys. Lett. **102**, 013116 (2013)

[5] Ehrhardt F.; Ulhaq-Bouillet C.; Muller D.; Slaoui A.; Ferblantier G., Incorporation of dopant impurities into a silicon oxynitride matrix containing silicon nanocrystals, J. Appl. Phys. **119**, 174303 (2016)

[6] König D.; Gutsch S.; Gnaser H.; Wahl M.; Kopnarski M.; Göttlicher J.; Steininger R.; Zacharias M.; Hiller D., Location and electronic nature of Phosphorus in the Si nanocrystal-SiO_2 system, Sci. Rep. **5**, 09702 (2015)

[7] Pi X.; Delerue C., Tight-binding calculations of the optical response of optimally P-doped Si nanocrystals: a model for localized surface plasmon resonance, Phys. Rev. Lett. **111**, 177402 (2013)

[8] Rowe D. J.; Jeong J. S.; Andre Mkhoyan K.; Kortshagen U. R, Phosphorus-doped Si nanocrystals exhibiting mid-infrared localized surface plasmon resonance, Nano Letters **13**, 1317 (2013)

[9] Kramer N. J.; Schramke K. S.; Kortshagen U. R., Plasmonic properties of silicon nanocrystals doped with boron and phosphorus, Nano Letters **15**, 5597 (2015)

[10] Zhou S.; Pi X.; Ni Z.; Ding Y.; Jin C.; Delerue C.; Yang D.; Nozaki T., Comparative study on the localized surface plasmon resonance of boron- and phosphorus-doped silicon nanocrystals, ACS Nano **9**, 378 (2015)

[11] Zhou S.; Pi X.; Ni Z.; Luang Q.; Jiang Y.; Jin C.; Nozaki T.; Yang D., Boron- and phosphorus-hyperdoped silicon nanocrystals, Part. Part. Syst. Charact **32**, 213 (2015)

[12] Olesinski R. W.; Kanani N.; Abbaschian G. J., The P-Si (Phophorus-Silicon) system Bulletin of Alloy Phase Diagrams **6**, 130-133 (1985)

[13] Safarian J.; Tangstad M., Phase diagram study of the Si-P system in Si-rich region, J. Mat. Research **26**, 1494-1503 (2011)

[14] Liang S. M.; Schmid-Fetzer R., Modeling of thermodynamic properties and phase equilibria of the Si-P system, J. of Phase Equilibria and Diffusion **35**, 24-35 (2014)

[15] Wadsten T., The crystal structures of SiP_2, $SiAs_2$ and GeP, Acta Chem. Scand. **21**, 593-594 (1967)

[16] Wadsten T., Synthesis of a pyrite type modification of SiP_2, Acta Chem. Scand. **21**, 1374-1376 (1967)

[17] Donohue P. C.; Siemons W. J.; Gillson J. L., Preparation and properties of pyrite-type SiP_2 and $SiAs_2$, J. Phys. Chem. Solids **29**, 807-813 (1968)

[18] Farberovich O. V.; Domashevskaya E. P., Band structure and density of states in SiP_2, Phys. Stat. Sol. B **72**, 662-665 (1975)

[19] Vogt H.; Chattopadhyay T.; Stolz H. J., Complete first order Raman spectra of the pyrite structure compounds FeS_2, MnS_2 and SiP_2, J. Phys. Chem. Solids **44**, 869-874 (1983)

[20] Meier M.; Weihrich R., Ab initio simulation of the fundamental vibrational frequencies of selected pyrite-type pnictides, Chem. Phys. Letters **461**, 38-41 (2008)

[21] Bachhuber F.; Rothballer J.; Pielnhofer F.; Weihrich R., First principles calculations on structure, bonding and vibrational frequencies of SiP_2, The Journal of Chemical Physics **135**, 124508 (2011)

[22] SpringThorpe A. J., The preparation of single crystal orthorhombic SiP_2, Mat. Res. Bull. **4**, 125-1278 (1969)

[23] Zhang X.; Wang S.; Ruan H.; Zhang G.; Tao X., Structure and growth of single crystal SiP_2 using flux method, Solid State Sciences **37**, 1-5 (2014)

[24] Kwon H. T.; Lee C. K.; Jeon K .J.; Park C. M., Silicon diphosphide: a Si-based 3D crystalline framework as a high performance Li-ion battery anode, ACS Nano **10**, 5701-5709 (2016)

[25] Wang C. Y.; Yi Y. H.; Chang W. C.; Kao T. L.; Tuan H.Y., Multi walled carbon nanotube-wrapped SiP_2 as a superior anode material for lithium-ion and sodium-ion batteries, J. of Power Sources **399**, 49-58 (2018)

[26] Reinhold R.; Stoeck U.; Grafe H. J.; Mikhailova D.; Jaumann T.; Oswald S.; Kaskel S.; Giebeler L., Surface and electrochemical studies on silicon diphosphide as easy-to-handle anode material for lithium-based batteries-the phosphorus path, ACS Applied Materials and Interfaces **10**, 7096-7106 (2018)

[27] Saddique J.; Zhang X.; Wu T.; Wang X.; Cheng X.; Su H.; Liu S.; Zhang L., Li G.; Zhang Y.; Yu H, Enhanced silicon diphosphide-carbon composite anode for long cycle, high efficient sodium ion batteries, ACS Applied Energy Materials **2**, 2223-2229 (2019)

[28] Huang B.; Zhuang H. L.; Yoon M.; Sumpter B. G.; Wei S. H., Highly stable two-dimensional silicon phosphides: different stoichiometries and exotic electronic properties, Phys. Rev. B **91**, 121401 (R) (2015)

[29] Zhang S.; Guo S.; Huang Y.; Zhu Z.; Cai B; Xie M.; Zhou W.; Zeng H., Two dimensional SiP: an unexplored direct band-gap semiconductor, 2D Materials **4**, 015030 (2017)

[30] Malyi O.I.; Sopiha K. V.; Radchenko I.; Wu P.; Persson C., Tailoring electronic properties of multilayer phosphorene by siliconization, Phys. Chem. Chem. Phys. 20, 2075 (2018)

[31] Matta S. K.; Zhang C.; Jiao Y.; O'Mullane A.; Du A., Versatile two-dimensional silicon diphosphide (SiP_2) for photocatalytic water splitting, Nanoscale **10**, 6369 (2018)

[32] Lippert G.; Osten H. J.; Krüger D.; Gaworzewski P.; Eberl K., Heavy phosphorus doping in molecular beam epitaxial grown silicon with a GaP decomposition source, Appl. Phys. Lett. **66**, 3197 (1995)

[33] Dovesi R.; Orlando R.; Erba A.; Zicovich-Wilson C. M.; Civalleri B.; Casassa S.; Maschio S.; Ferrabone M.; De La Pierre M.; D'Arco P.; Noël Y.; Causà M.; Rérat M.; Kirtman B., CRYSTAL 14 : a program for the *ab initio* investigation of crystalline solids, Int. J. Quantum Chem. **114**, 1287-1317 (2014)

[34] Becke A. D., Density-functional thermochemistry.III.The role of exact exchange, The Journal of Chemical Physics **98**, 5648-5652 (1993)

[35] Peintinger M. F.; Vilela Oliveira D.; Bredow T., Consistent Gaussian basis sets of triple-zeta valence with polarization quality for solid-state calculations, Journal of Computational Chemistry **34**, 451-459 (2013)

[36] Wu R. J.; Topsakal M.; Low T.; Robbins M. C.; Haratipour N.; Jeong J. S.; Wentzcovitch R. M.; Koester S .J.; Mkhoyan K .A., Atomic and electronic structure of exfoliated black phosphorus, J. Vac. Sci. and Technol. A **33**, 060604 (2015)

[37] Mimura A.; Fujii M.; Hayashi S.; Kovalev D.; Koch F., Photoluminescence and free-electron absorption in heavily phosphorus-doped Si nanocrystals, Phys. Rev. B **62**, 12625 (2000)

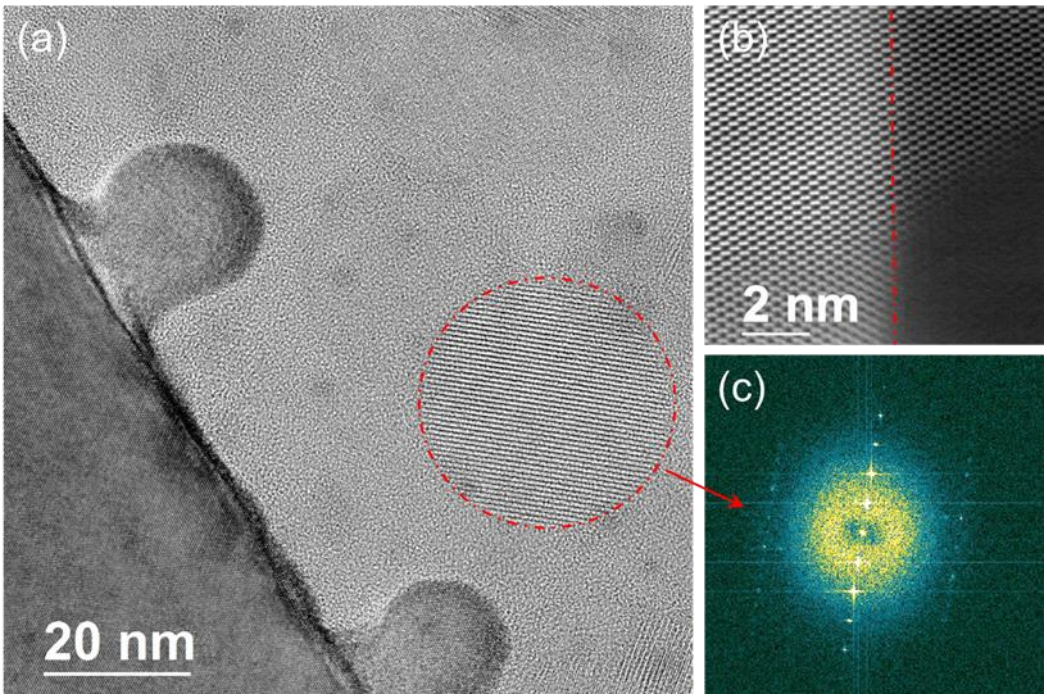

Fig.1

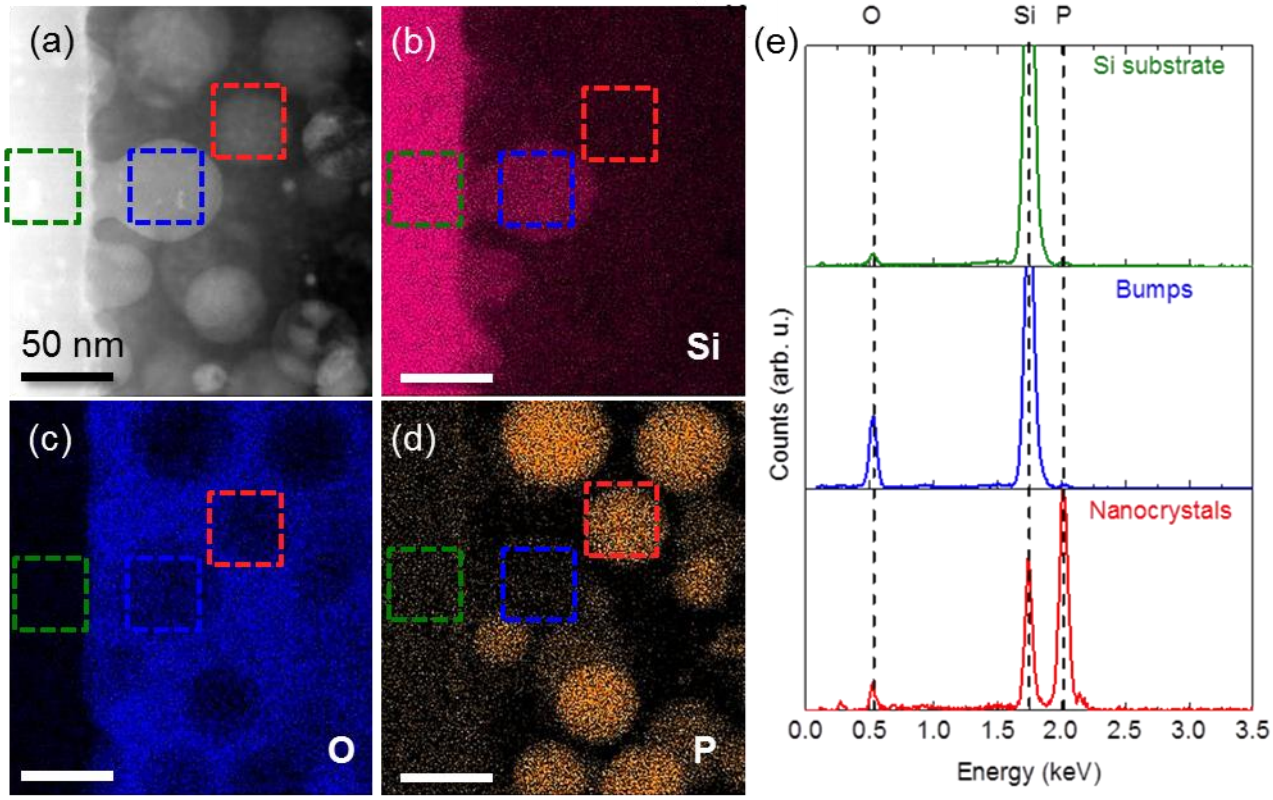
(a)
50 nm
(b)
Si
(c)
O
(d)
P
(e)
O
Si
P
Si substrate
Bumps
Nanocrystals
Counts (arb. u.)
0.0
0.5
1.0
1.5
2.0
2.5
3.0
3.5
Energy (keV)

Fig.2

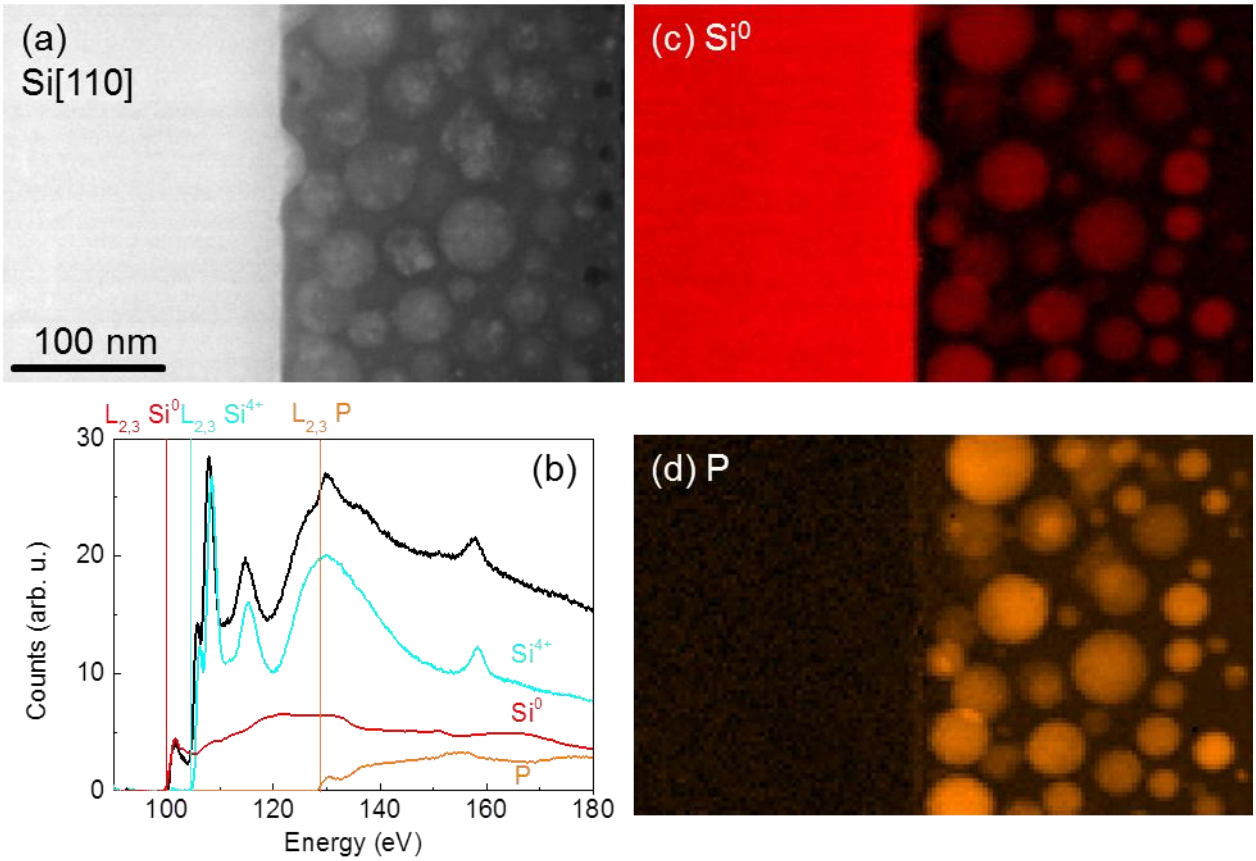
(a)
Si[110]
100 nm
(c) Si0
L2,3 Si0 L2,3 Si4+ L2,3 P
(b)
Counts (arb. u.)
Energy (eV)
Si4+
Si0
P
(d) P

Fig.3

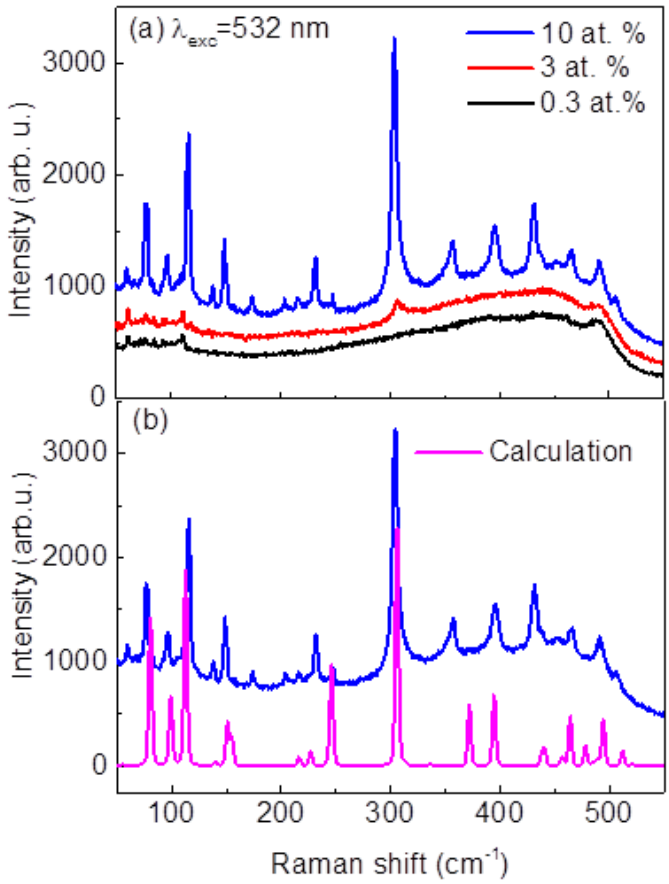
(a) λexc=532 nm
10 at. %
3 at. %
0.3 at.%
Intensity (arb. u.)
3000
2000
1000
0
(b)
Calculation
Intensity (arb.u.)
3000
2000
1000
0
100
200
300
400
500
Raman shift (cm-1)

Fig.4

ω_{DFT} (cm^{-1})	ω_{EXP} (cm^{-1})	ω_{DFT} (cm^{-1})	ω_{EXP} (cm^{-1})
80 (Ag)	77	306 (Ag)	304
99 (B1g)	96	371 (Ag)	356
112 (Ag)	115	394 (B3g)	395
139 (B1g)	138	439 (Ag)	431
150 (B3g)	149	456 (B1g)	452
187 (B2g)	173	464 (Ag)	465
216 (B1g)	203	477 (Ag)	478
226 (Ag)	216	494 (Ag)	490
245 (B1g)	231	511 (B1g)	506

Table I

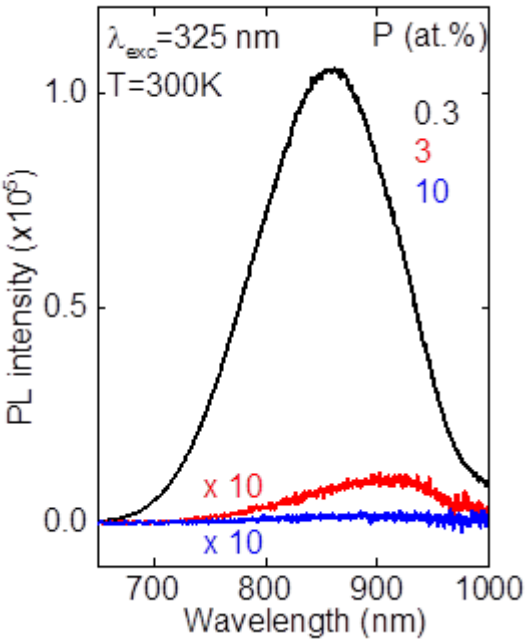
λexc=325 nm
T=300K
P (at.%)
0.3
3
10
x 10
x 10
PL intensity (x10^5)
1.0
0.5
0.0
700
800
900
1000
Wavelength (nm)

Fig. 5